Rationalization of the structural, electronic and photophysical properties of silver(I) halide n-picolylamine hybrid coordination polymers.

Caterina Zuffa,[a] Daniele Veclani,[b] Marianna Marchini,[a] Filippo Monti,*[b]

Chiara Cappuccino,[a†] Lucia Maini,*[a] and Barbara Ventura[b]

[a] Università di Bologna, Dipartimento di Chimica ‘‘Giacomo Ciamician”, 40126, Bologna, Italy.

[b] Consiglio Nazionale delle Ricerche, Istituto per la Sintesi Organica e la Fotoreattività (CNR–ISOF), Via Piero Gobetti 101, 40129 Bologna, Italy.

[†] C.C. now at Chemistry Department, Brookhaven National Laboratory, Brookhaven, NY, USA.

Table of Contents

Crystallographic information

Table S1. Crystal data and structure refinement for $[(AgBr)(n\text{-pica})]_n$ coordination polymers[1], reported for sake of clarity.

	$[(AgBr)(2\text{-pica})]_n$	**$[(AgBr)(3\text{-pica})]_n$**	**$[(AgBr)(4\text{-pica})]_n$**
Empirical formula	$C_6H_8AgBrN_2$	$C_6H_8AgBrN_2$	$C_6H_8AgBrN_2$
Formula weight (g mol^{-1})	295.915	295.915	295.915
T (K)	293	293	293
Wavelength (Å)	0.71073	0.71073	1.535
Crystal system	triclinic	monoclinic	monoclinic
Space group	P-1	$P2_1/c$	$P2_1/c$
a (Å)	4.3871(5)	9.4518(6)	6.316(1)
b (Å)	10.1081(12)	6.1880(3)	7.365(1)
c (Å)	10.2510(18)	14.3981(9)	17.769(1)
α (°)	113.498(14)	90	90
β (°)	97.081(12)	105.712(6)	81.08(1)
γ (°)	93.535(9)	90	90
V (Å^3)	410.63(11)	810.64(8)	816
Z, Z’	2, 1	4, 1	4, 1
ρ_{calc} (mg m^{-3})	2.393	2.425	2.407

Table S2. Crystal data and structure refinement for $[(AgCl)(n\text{-pica})]_n$ coordination polymers.

	$[(AgCl)(2\text{-pica})]_n$	**$[(AgCl)(3\text{-pica})]_n$**	**$[(AgCl)(4\text{-pica})]_n$**
Empirical formula	$C_6H_8AgClN_2$	$C_6H_8AgClN_2$	$C_6H_8AgClN_2$
Formula weight (g mol^{-1})	251.46	251.46	251.46
T (K)	293	293	293
Wavelength (Å)	0.71073	0.71073	1.535
Crystal system	orthorhombic	monoclinic	monoclinic
Space group	$P2_12_12_1$	$P2_1$	$P2_1/c$
a (Å)	6.5423(4)	9.2824(6)	6.186(1)
b (Å)	7.0698(5)	6.0256(3)	7.248(1)
c (Å)	17.3926(10)	7.3134(5)	17.40(1)
α (°)	90	90	90
β (°)	90	108.918(8)	82.05(1)
γ (°)	90	90	90
V (Å^3)	804.46(9)	386.96(4)	772.62
Z, Z’	4, 1	2, 1	4, 1
ρ_{calc} (mg m^{-3})	2.076	2.158	2.162
μ (mm^{-1})	2.760	2.869	
F(000)	488	244	
crystal size (mm)	0.144x0.127x0.057	0.153x0.124x0.044	powder
θ range for data collection (◦)	3.327° to 29.248°	4.102° to 28.898°	9.5° to 70°
reflections collected	2384	2965	
Independent reflections	1603	1647	
R_{int}/R-Bragg	0.0235	0.0353	0.0114
Completeness to theta = 25.000°	99.7%	99.6%	
Refinement method	Full-matrix least-squares on F^2	Full-matrix least-squares on F^2	Rietveld
Tmax/Tmin	1.00000/ 0.87046	1.00000/0.91766	
data/restraints/parameters	1603/0/91	1647/1/92	
Goodness-of-fit on F^2	0.999	1.030	1.771
R1 [I > 2σ(I)]/Rp	0.0428	0.0470	0.0317
*w*R2 (all data)/Rwp	0.0683	0.0767	0.0437

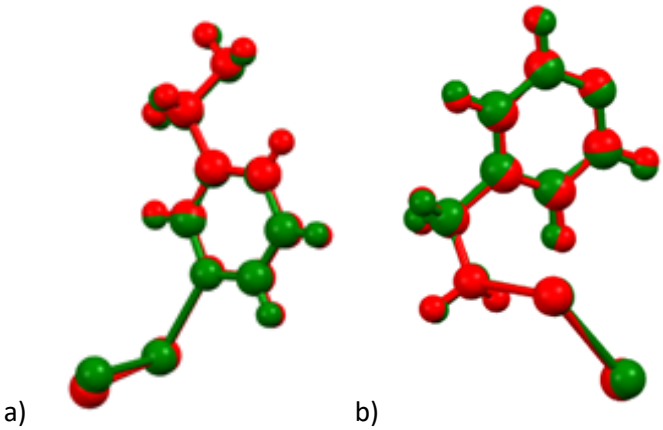

Fig. S1 asymmetric unit overlay of a) $[(AgCl)(3\text{-pica})]_n$ and $[(AgBr)(3\text{-pica})]_n$ and b) $[(AgCl)(4\text{-pica})]_n$ and $[(AgBr)(4\text{-pica})]_n$. The structures AgCl-based are in green, the AgBr-based ones are in red.

Table S3. Isostructurality parameters of $[(AgX)(3\text{-pica})]_n$ and $[(AgX)(4\text{-pica})]_n$

	π	Is	RMSD	Max D
3-pica	0.248	84%	0.180	0.278
4-pica	0.019	98%	0.0995	0.138

$[Ag(H4\text{-pica})Cl_2)]_n$

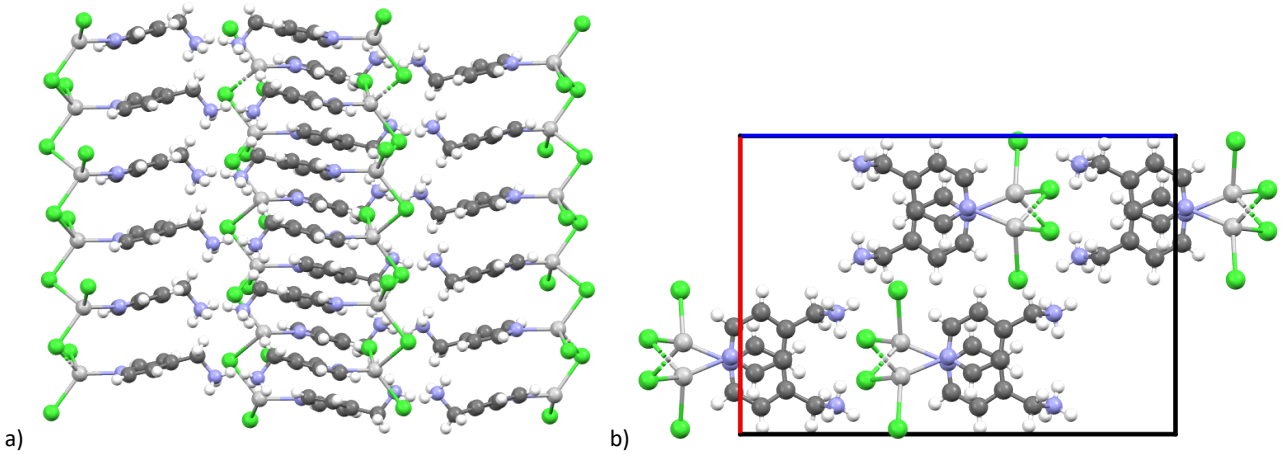

Fig. S1 a) $[Ag(H4\text{-pica})Cl_2]_n$ structure; b) packing along b-axis

Table S4. Crystal data and structure refinement for $[Ag(H4\text{-}pica)Cl_2]_n$.

	$[Ag(H4\text{-}pica)Cl_2]_n$
Empirical formula	$C_6H_9N_2AgCl_2$
Formula weight (g mol^{-1})	287.92
T (K)	293
Wavelength (Å)	0.71073
Crystal system	orthorhombic
Space group	Pbca
a (Å)	13.2106(4)
b (Å)	7.0400(3)
c (Å)	19.2703(5)
α (°)	90
β (°)	90
γ (°)	90
V ($Å^3$)	1792.19
Z, Z’	8, 1
ρ_{calc} (mg m^{-3})	2.134
μ (mm^{-1})	2.781
F(000)	1120
crystal size (mm)	0.187x0.127x0.093
θ range for data collection (◦)	3.445° to 29.225°
reflections collected	25352
Independent reflections	2246
R_{int}	0.0347
Completeness to theta = 25.000°	99.8%
Refinement method	Full-matrix least-squares on F^2
Tmax/Tmin	1.00000/0.61123
data/restraints/parameters	2246/0/101
Goodness-of-fit on F^2	1.147
R1 [I > 2σ(I)]	0.0431
*w*R2 (all data)	0.0833

PXRD patterns

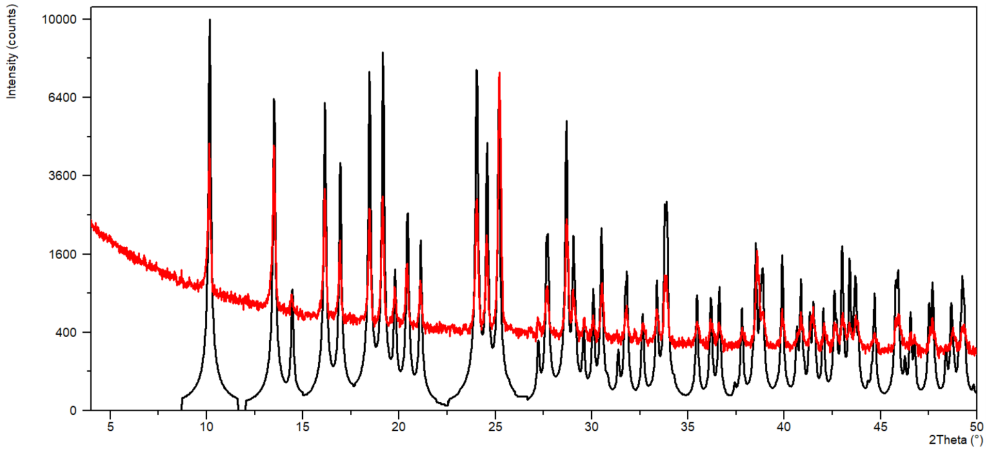

Fig. S3 Comparison between calculated (black line) and experimental (red line) X-ray powder diffraction patterns of $[(AgCl)(2\text{-pica})]_n$. The diffractograms are shown in square root intensity mode.

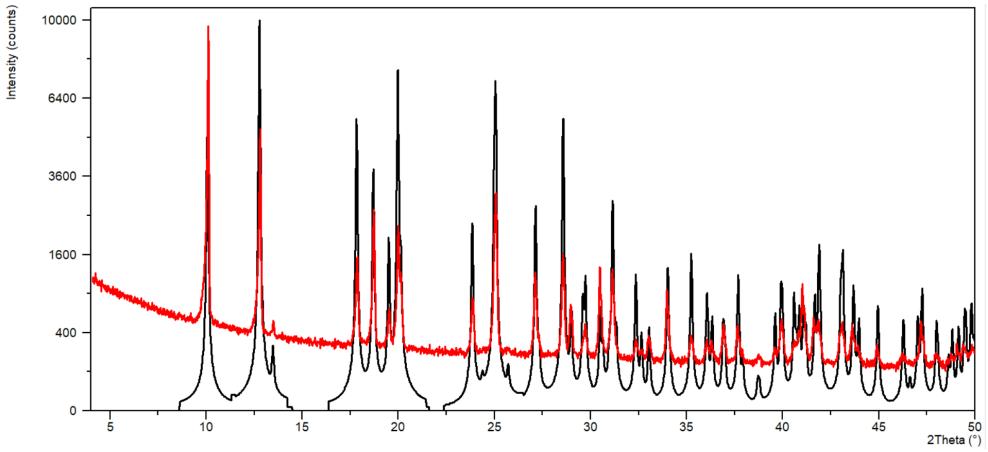

Fig. S4 Comparison between calculated (black line) and experimental (red line) X-ray powder diffraction patterns of $[(AgCl)(3\text{-pica})]_n$. The diffractograms are shown in square root intensity mode.

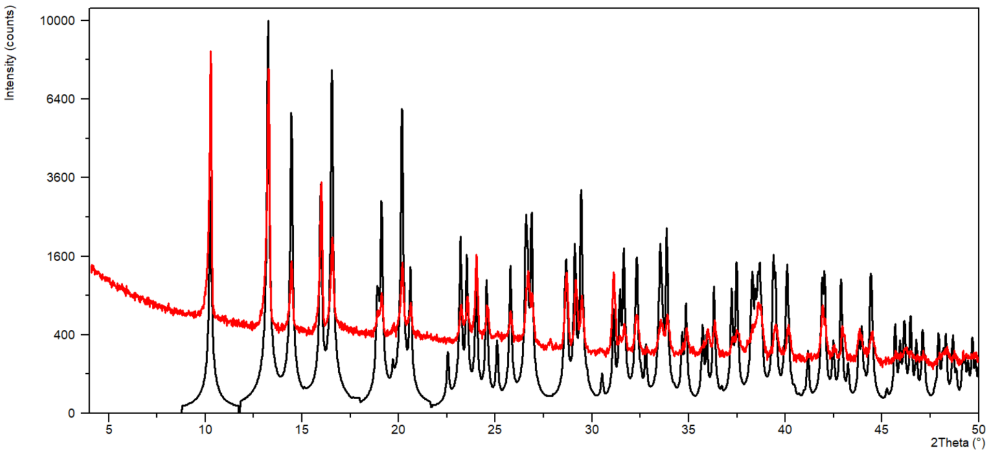

Fig. S5 Comparison between calculated (black line) and experimental (red line) X-ray powder diffraction patterns of $[(AgCl)(4\text{-pica})]_n$. The diffractograms are shown in square root intensity mode.

DFT calculations

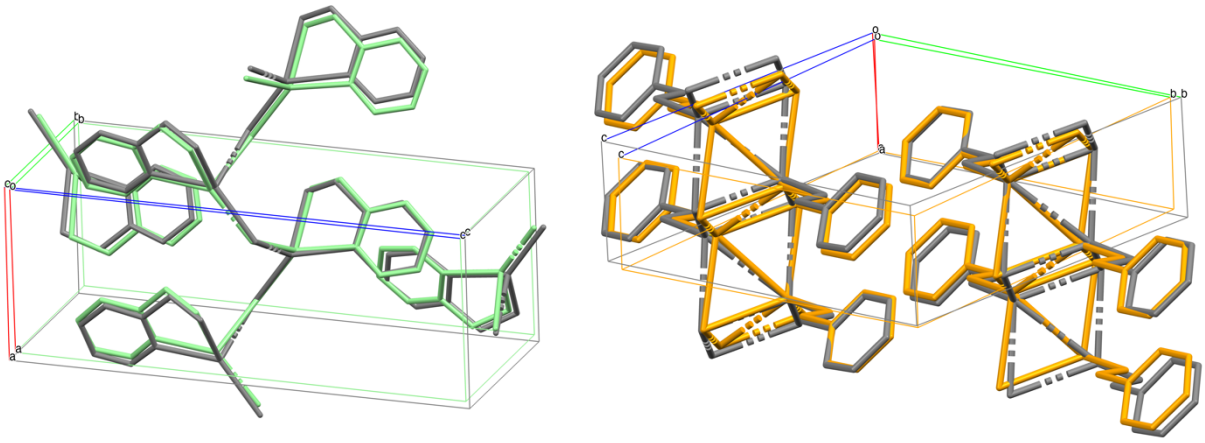

Fig. S6 Structural overlap (obtained by maximising the superpositions of silver atoms) between experimental (gray) and DFT-optimized structures of $[(AgCl)(2\text{-pica})]_n$ (left, green) and $[(AgBr)(2\text{-pica})]_n$ (right, orange).

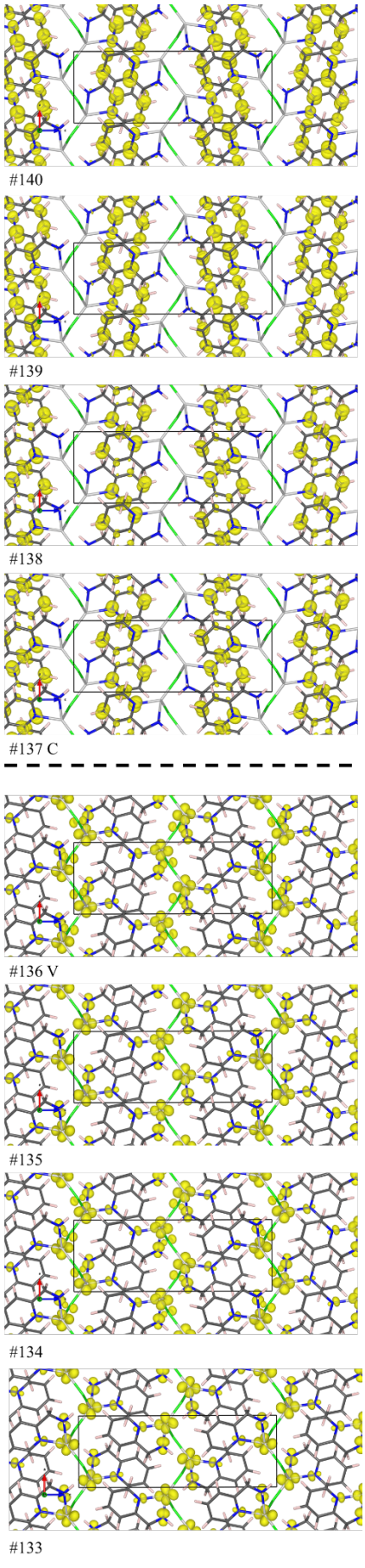

Fig. S7 Orbital densities associated to selected wavefunctions in Γ reciprocal space for the highest four valence and lowest four conduction bands of $[(AgCl)(2\text{-pica})]_n$ (isosurfaces are plotted at 0.002 a.u.).

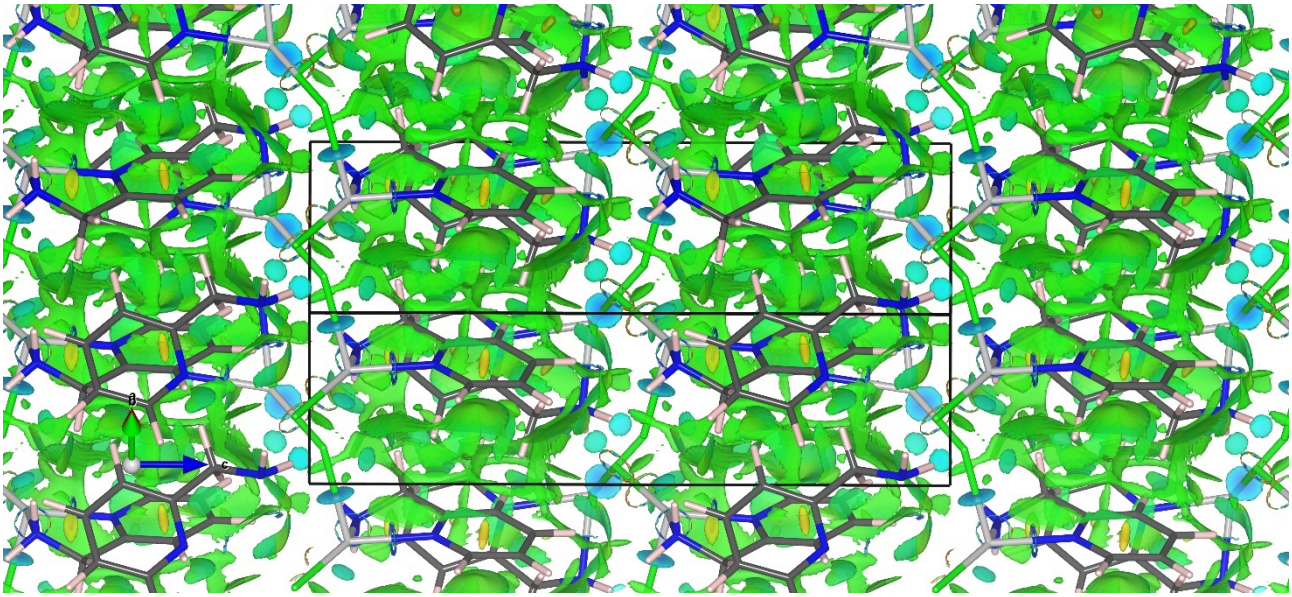

Fig. S8 View of the $[(AgCl)(2\text{-pica})]_n$ crystal showing the reduced gradient density isosurfaces at 0.40 a.u., mapped using the product of the electron density and the second eigenvalue of the electron-density Hessian matrix (green coloured regions indicate non-covalent interactions). Interdigitated 2-pica ligands chelating different inorganic chains interact with each other *via* van-der-Waals interactions.

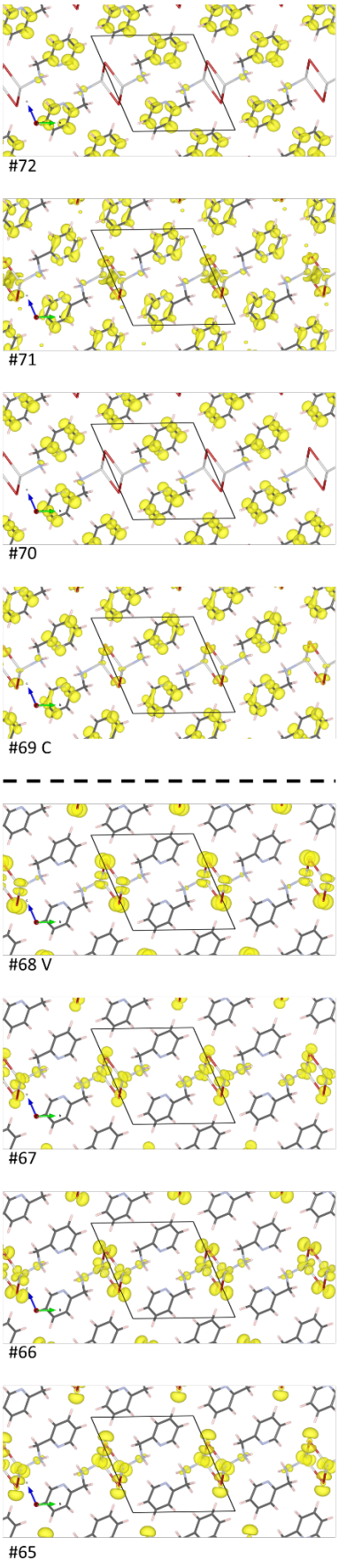

Fig. S9 Orbital densities associated to selected wavefunctions in Γ reciprocal space for the highest four valence and lowest four conduction bands of $[(AgBr)(2\text{-pica})]_n$ (isosurfaces are plotted at 0.002 a.u.).

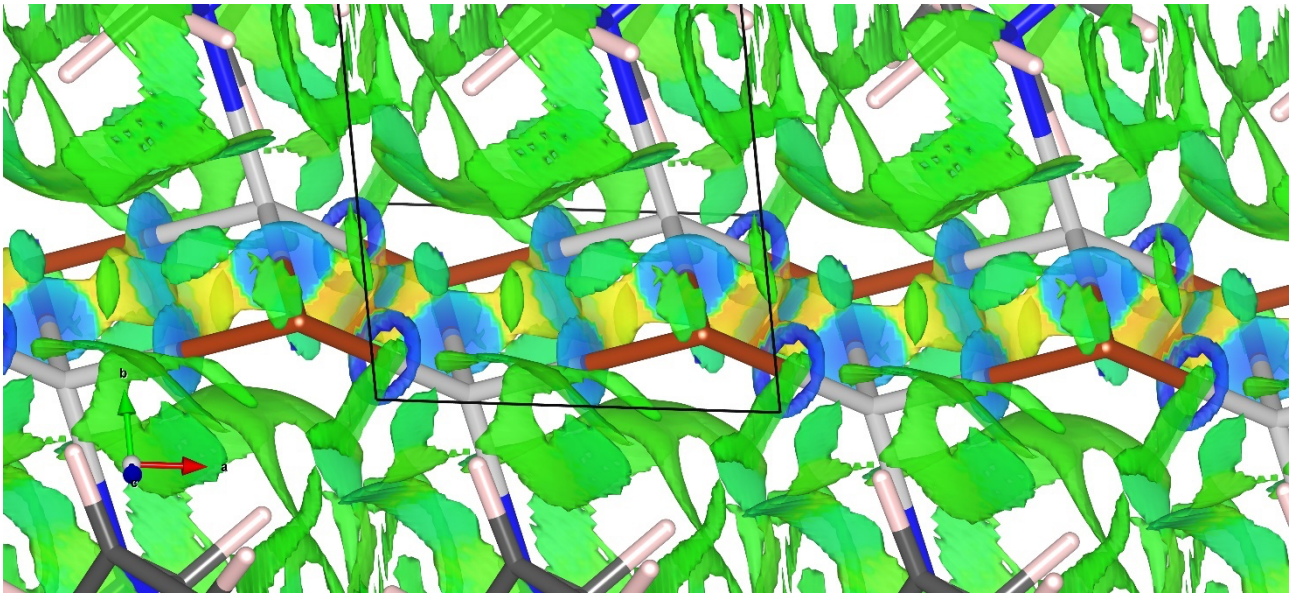

Fig. S10 Detail of the $[(AgBr)(2\text{-pica})]_n$ inorganic double chain with reduced gradient density isosurfaces at 0.33 a.u., mapped using the product of the electron density and the second eigenvalue of the electron-density Hessian matrix (colours span from red to blue, indicating repulsive or attractive interactions, respectively). Two kinds of argentophilic interactions are clearly visible at the centre of each Ag_2Br_2 ring.

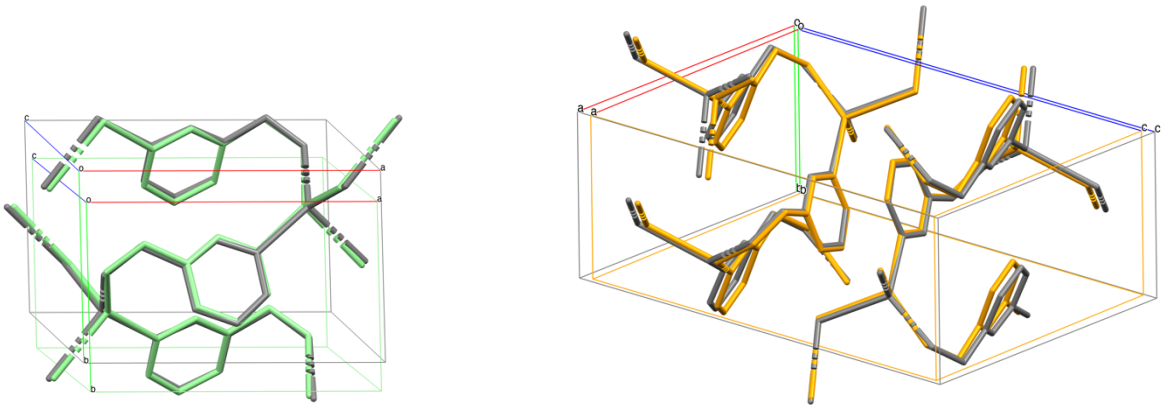

Fig. S11 Structural overlap (obtained by maximising the superpositions of silver atoms) between experimental (gray) and DFT-optimized structures of $[(AgCl)(3\text{-pica})]_n$ (left, green) and $[(AgBr)(3\text{-pica})]_n$ (right, orange).

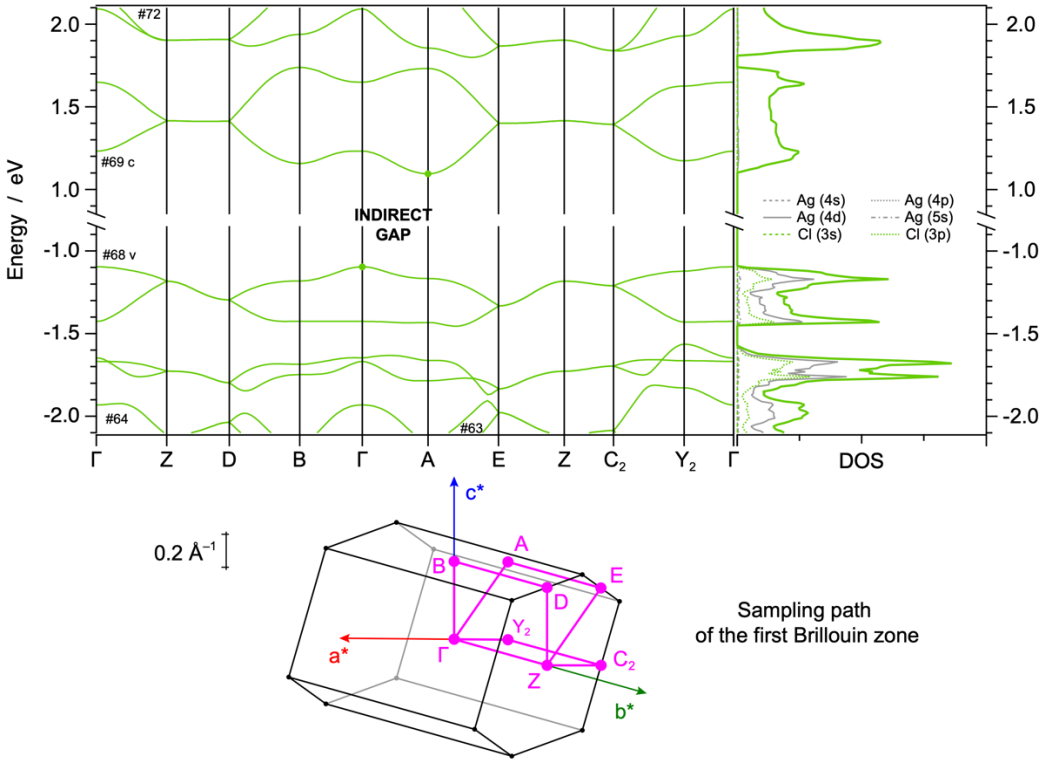

Fig. S12 Band-structure diagram and density-of-states (DOS) plot of $[(AgCl)(3\text{-pica})]_n$ with relative orbital contributions; the band-structure path in the reciprocal space (first Brillouin zone) is also depicted. All data refer to the standard cell of $[(AgCl)(3\text{-pica})]_n$ to be compared to the 1x1x2 supercell depicted in Figure 4, main text.

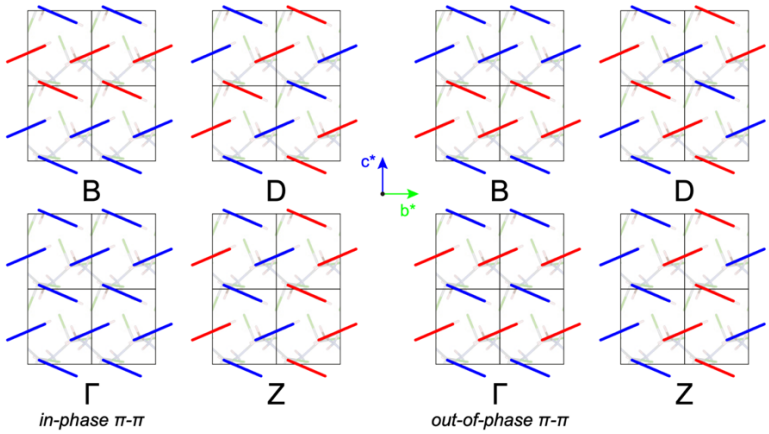

Fig. S13 Schematic 2-D representation of the π-interactions along the *bc* plane in $[(AgCl)(3\text{-pica})]_n$. Simplified analysis of the lowest couple of conduction bands. Each of the two band has, as basis, the in-phase or out-of-phase combination of the same lowest π* orbital centred on each of the two equivalent 3-pica ligands found in the primitive cell. For both bands, orbital contributions are sketched at Γ, B, Z and D *k*-points, showing how such bands become degenerate in Z and D. On the hand, despite in B the topological pattern is similar for both bands, no degeneracy is observed since the same kind of interaction occurs, in one case, within the same 2-D network (parallel to the *ab* plane) and, in the other, involving different nearby layers.

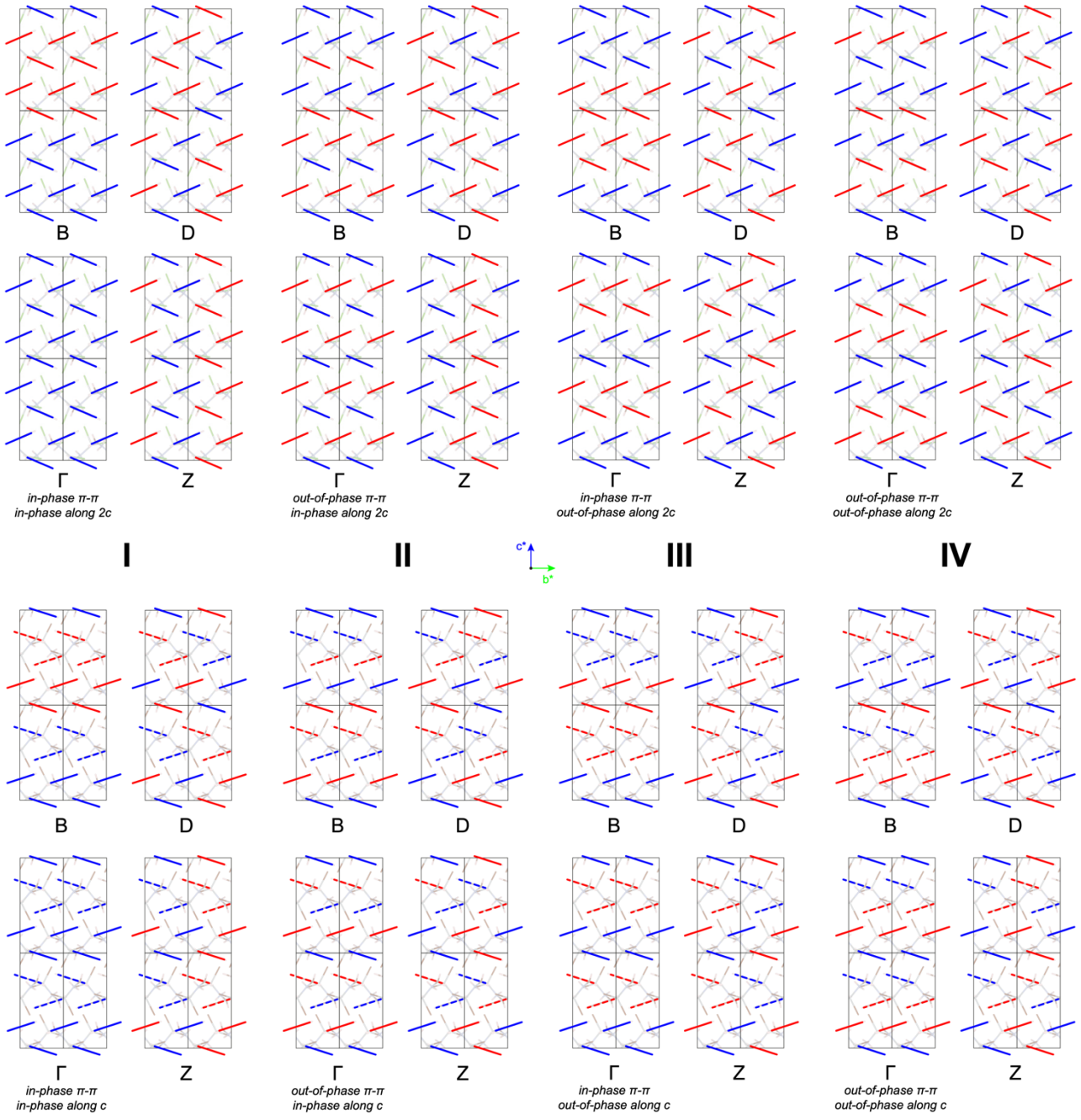

Fig. S14 Schematic 2-D representation of the π-interactions along the *bc* plane in $[(AgCl)(3\text{-pica})]_n$ (top) and $[(AgBr)(3\text{-pica})]_n$ (bottom). For the sake of clarity, a 1x1x2 supercell is used for $[(AgCl)(3\text{-pica})]_n$ crystal and the 3-pica π systems belonging to the inorganic helix of opposite chirality are dashed in $[(AgBr)(3\text{-pica})]_n$. The lowest four conduction bands (**I**–**IV**) are sketched as linear combinations of the same lowest π* orbital centred on each of the two couples of 3-pica ligands found in the crystal cells; the four linear combinations are obtained by an in-phase or out-of-phase mixing within each inorganic helix and in between the two helixes of the cells. For all bands, orbital contributions are sketched at Γ, B, Z and D *k*-points. In $[(AgCl)(3\text{-pica})]_n$, all bands become degenerate in Z and D due to the presence of equivalent helixes staked along *c*; the four-fold degeneracy is removed in $[(AgBr)(3\text{-pica})]_n$ since the two helixes of different chirality lead to a different rearrangement of the 3-pica ligands, leading to stronger π–π interactions within chains of opposite chirality (accordingly, just bands **I** and **III** are degenerate along Z–D–B, and the same occurs for **II** and **IV**).

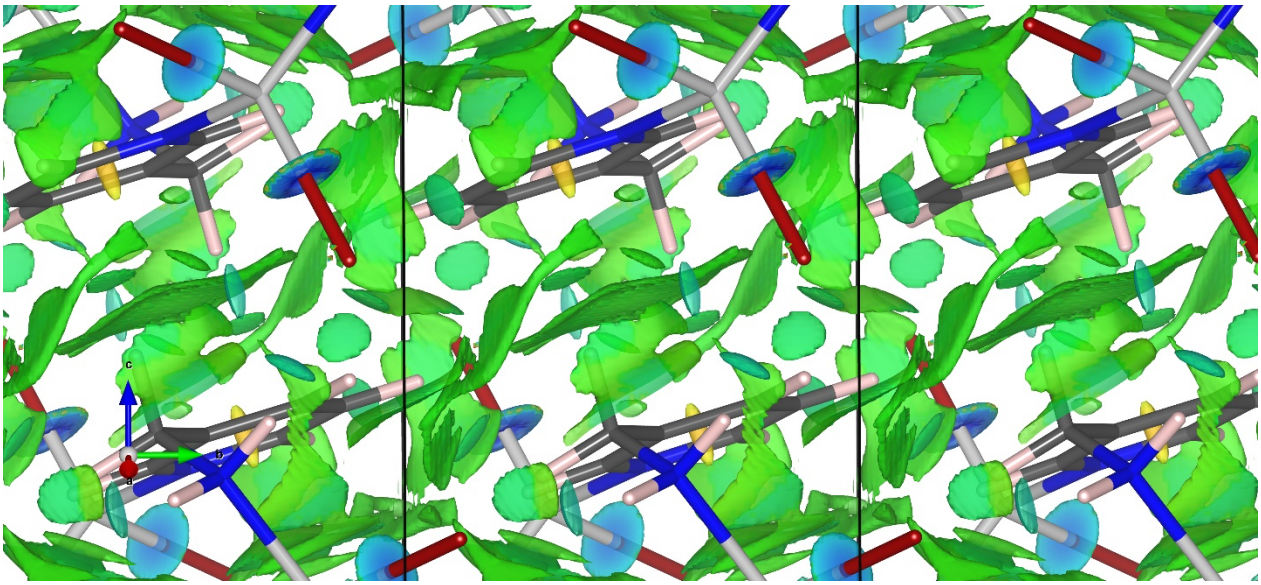

Fig. S15 View of the $[(AgBr)(3\text{-pica})]_n$ crystal showing the reduced gradient density isosurfaces at 0.40 a.u., mapped using the product of the electron density and the second eigenvalue of the electron-density Hessian matrix (green coloured regions indicate non-covalent interactions).

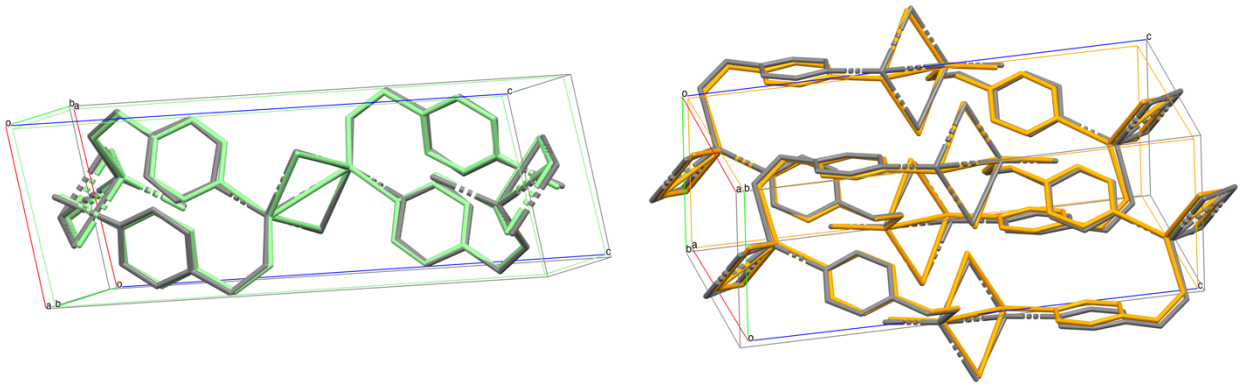

Fig. S16 Structural overlap (obtained by maximising the superpositions of silver atoms) between experimental (gray) and DFT-optimized structures of $[(AgCl)(4\text{-pica})]_n$ (left, green) and $[(AgBr)(4\text{-pica})]_n$ (right, orange).

a)

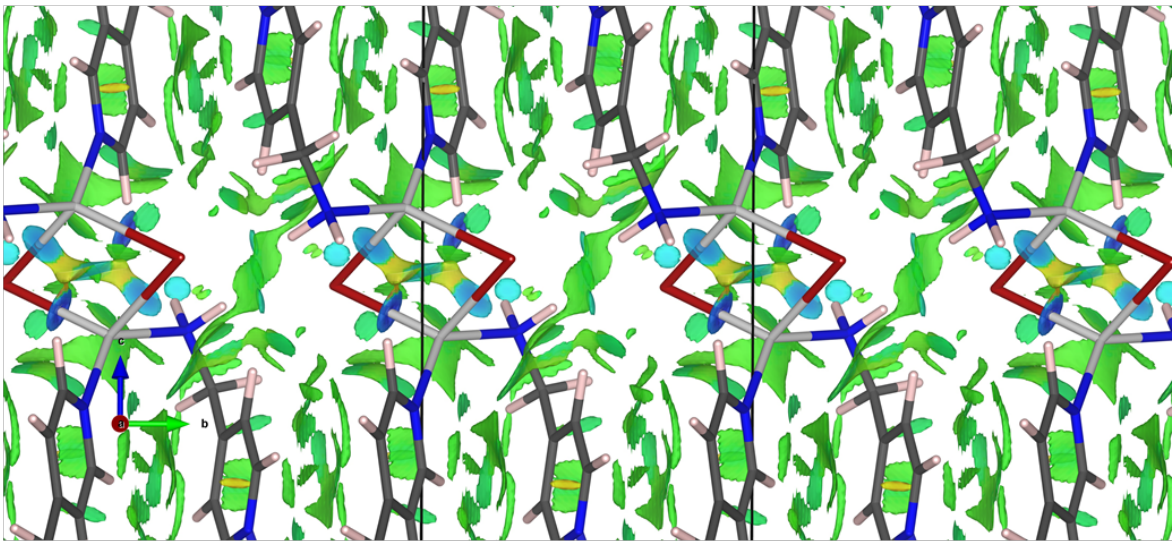

b)

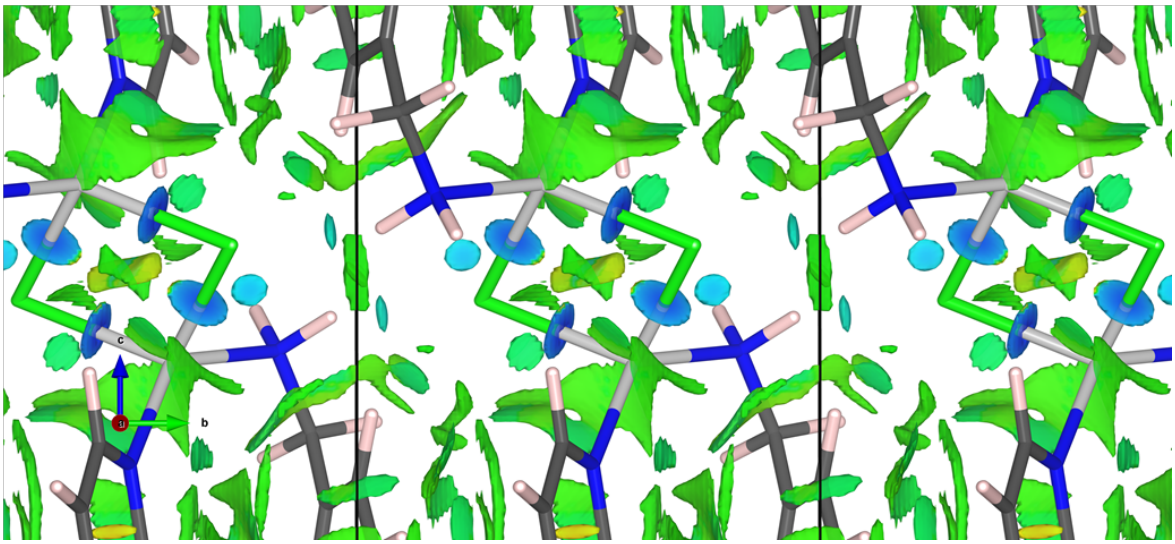

Fig. S17 View of the Ag_2X_2 unit in both a) $[(AgBr)(4\text{-pica})]_n$ and b) $[(AgCl)(4\text{-pica})]_n$ crystals along with the reduced gradient density isosurfaces at 0.33 a.u., mapped using the product of the electron density and the second eigenvalue of the electron-density Hessian matrix (colours span from red to blue, indicating repulsive or attractive interactions, respectively). The argentophilic interaction is clearly visible at the centre of each Ag_2X_2 ring.

Raman spectroscopy

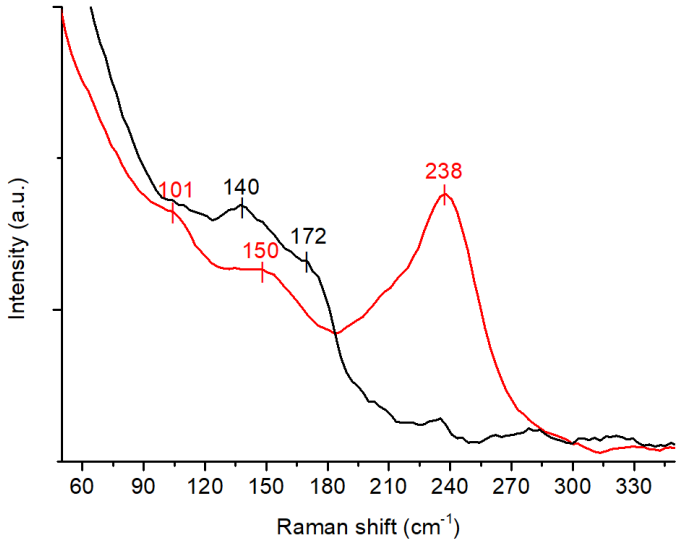

Fig. S18 Raman spectra of AgCl (red) and AgBr (black). For AgCl, the vibrational modes at 101 and 150 cm^{-1} correspond to the lattice vibrations of the silver (Ag) atoms within the crystal structure; the mode at 238 cm^{-1} is associated with the stretching vibrations of the Ag-Cl bonds located at the terminal positions of the crystal structure.[2] In the case of AgBr, similar to what is observed in AgCl, the low-wavelength mode at 140 cm^{-1} corresponds to the vibrational modes of the Ag lattice. The mode at 172 cm^{-1} is associated with the stretching of the Ag-Br bonds.[3]

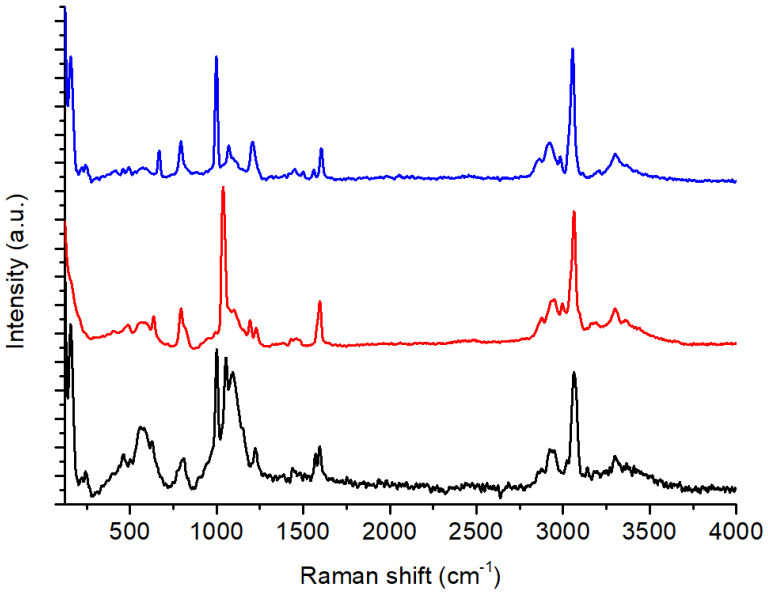

Fig. S19 Left: Raman spectra of 2-pica (black), 3-pica (red) and 4-pica (blue).

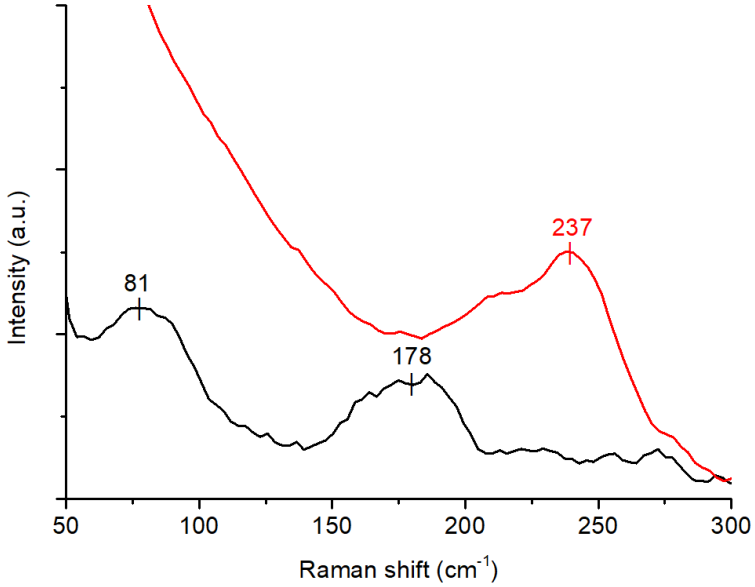

Fig. S20 Raman spectra of $[(AgCl)(2\text{-pica})]_n$ (red) and $[(AgBr)(2\text{-pica})]_n$ (black). The band at 81 cm^{-1} is ascribed to the presence of the metallophilic interactions.

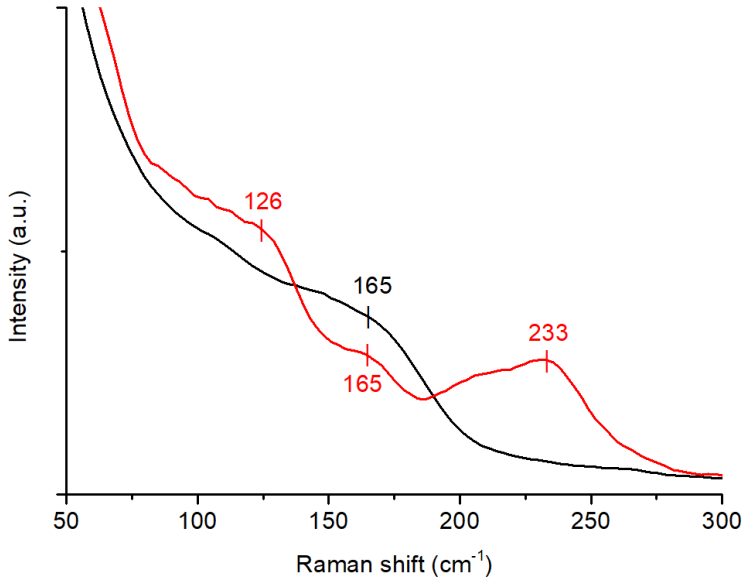

Fig. S21 Raman spectra of $[(AgCl)(3\text{-pica})]_n$ (red) and $[(AgBr)(3\text{-pica})]_n$ (black).

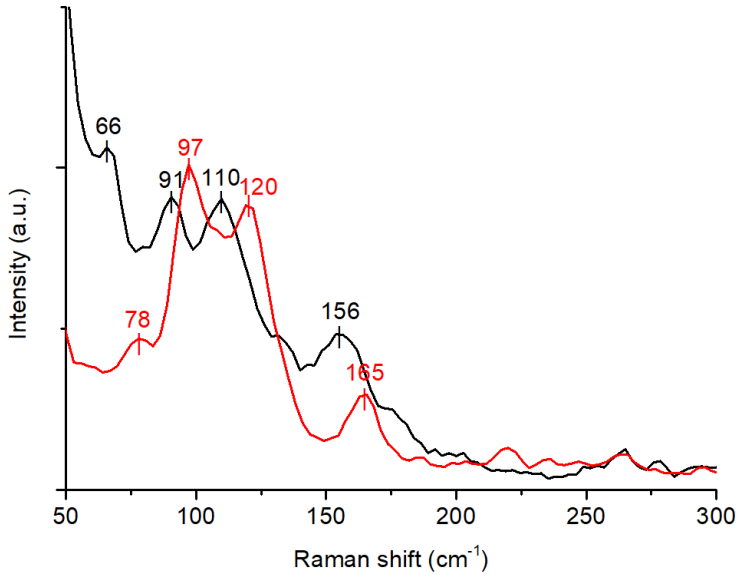

Fig. S22 Raman spectra of $[(AgCl)(4\text{-pica})]_n$ (red) and $[(AgBr)(4\text{-pica})]_n$ (black).

Rietveld refinement

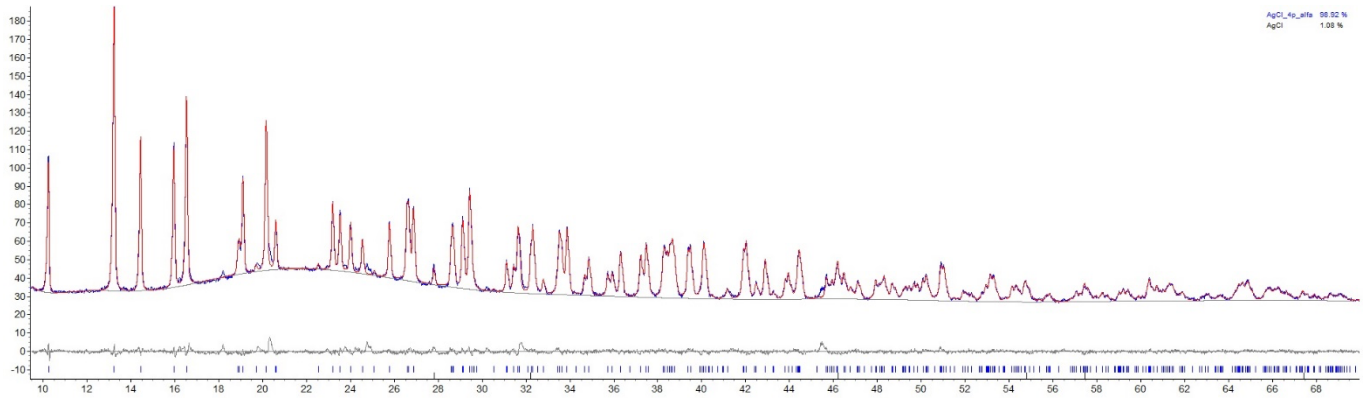

Fig. S23 Rietveld refinement (red line) on $[(AgCl)(4\text{-pica})]_n$ diffraction pattern (blue line). Peaks of unreacted AgCl are present. In grey, the difference plot.

Thermogravimetric analysis

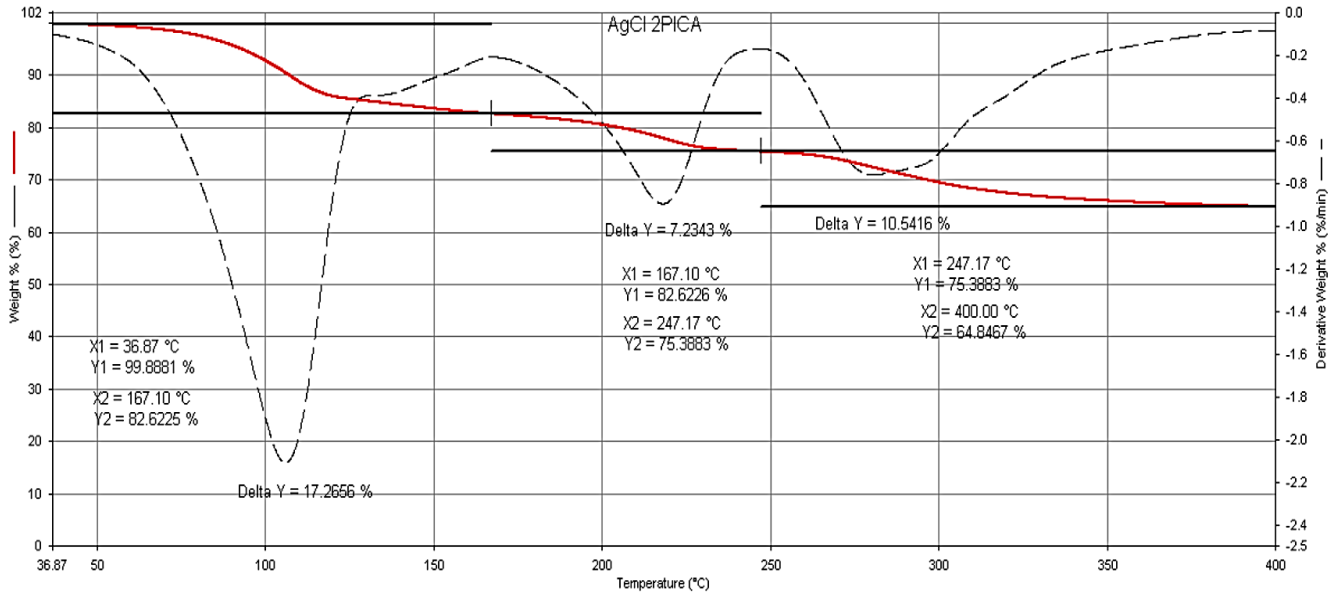

Fig. S24 TGA analysis of $[(AgCl)(2\text{-pica})]_n$. The partial release of 2-pica starts at temperatures higher than 50°C, while the melting point is observed at 70°C. The first weight lost (50°-150°C) is ascribable only to partial release of the 2-pica. At temperatures higher than 350°C the residual weight correspond to the AgCl (analysis 65% calc. 57%, the higher experimental value could be due to the presence of unreacted AgCl).

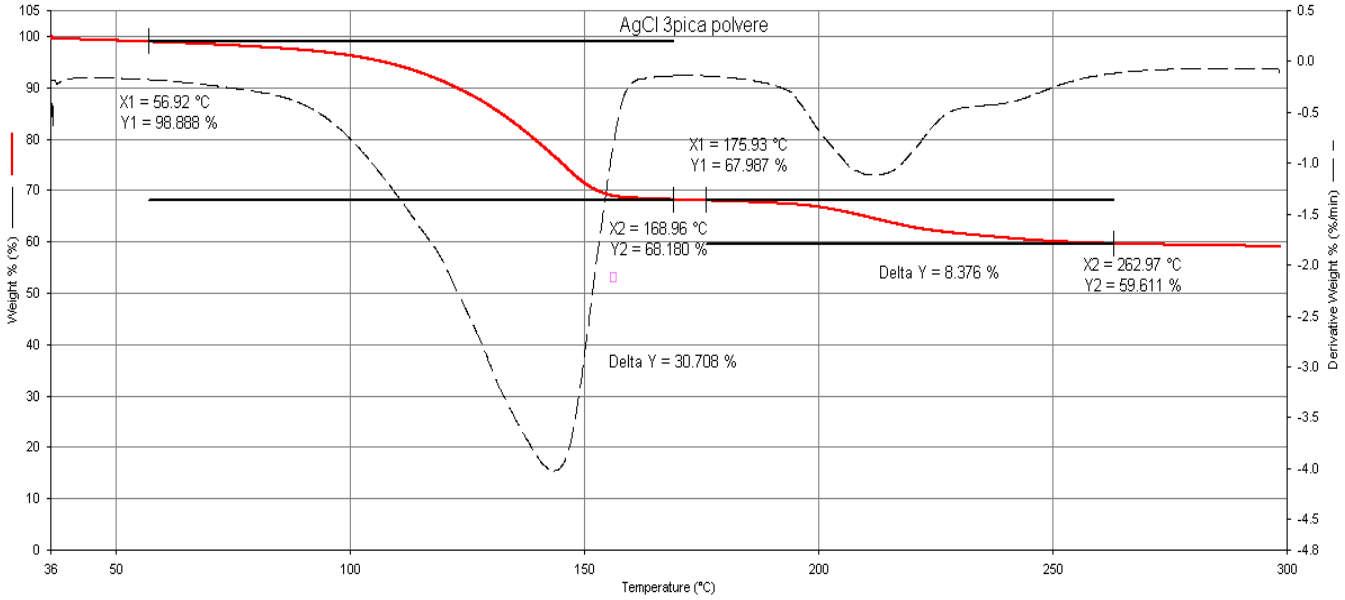

Fig. S25 TGA analysis of $[(AgCl)(3\text{-pica})]_n$. The weight loss can be ascribed to the loss of the 3-pica after melting (see figure S32). It is worth noting that the ligand is released in two different steps and at 250°C the residual powder is ascribable to the AgCl (analysis 60%, calc. 57%).

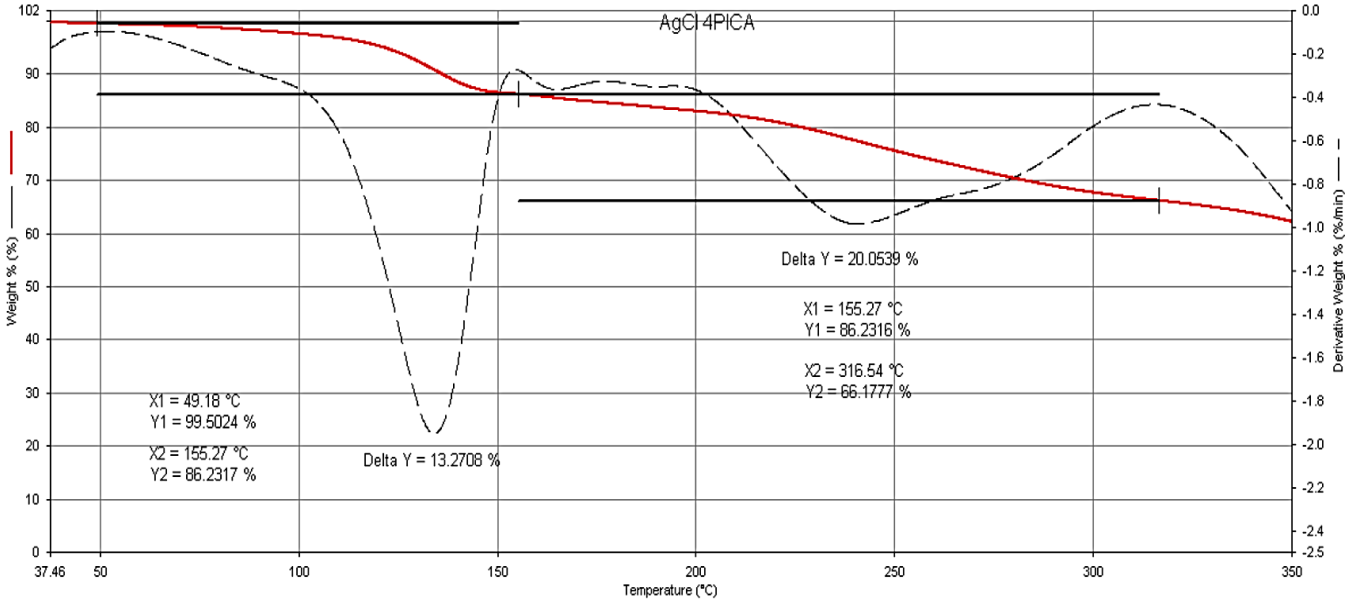

Fig. S26 TGA analysis of $[(AgCl)(4\text{-pica})]_n$. The first weight lost corresponds to the first endothermic peak and is ascribable to a partial release of the 4-pica. The full release of the ligand is observed at temperatures higher than 250°C.

Differential Scanning Calorimetry

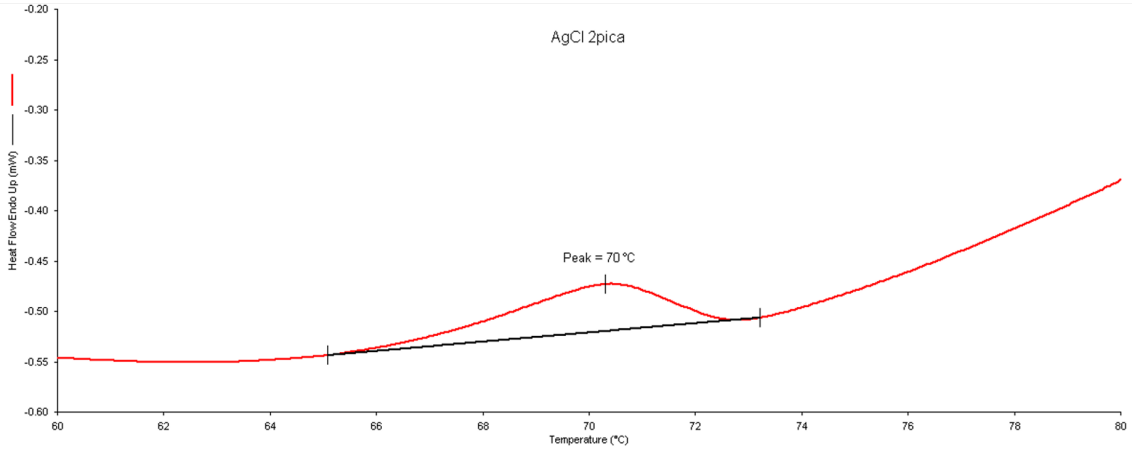

Fig. S27 DSC analysis of $[(AgCl)(2\text{-pica})]_n$. The endothermic peak at 70°C is due to the incongruent melting.

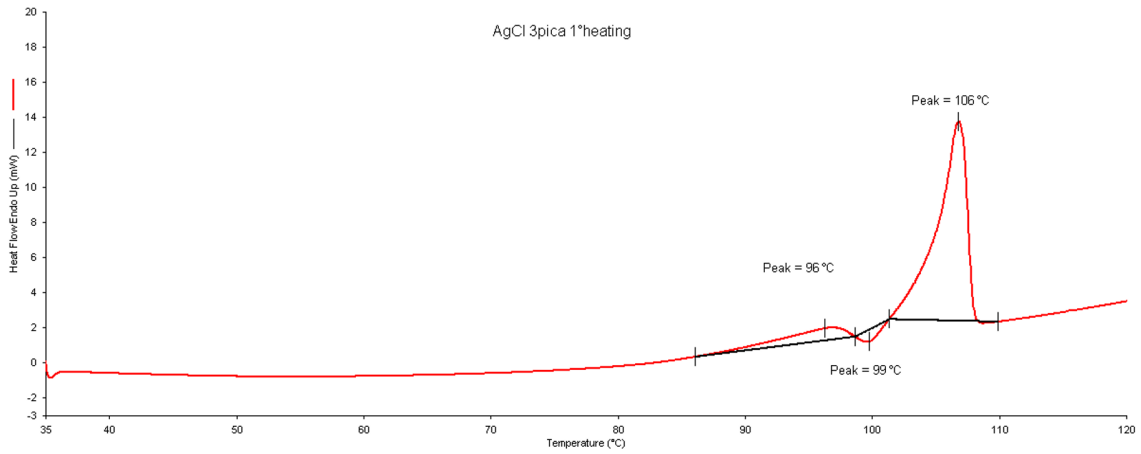

Fig. S28 DSC analysis of $[(AgCl)(3\text{-pica})]_n$. The endothermic peak at 96°C is followed by an exothermic peak (99°C) and then by another endothermic peak at 106°C. These events suggest a melting followed by recrystallization and a second melting peak. Further investigations are in progress to understand the thermal behaviour of $[(AgCl)(3\text{-pica})]_n$.

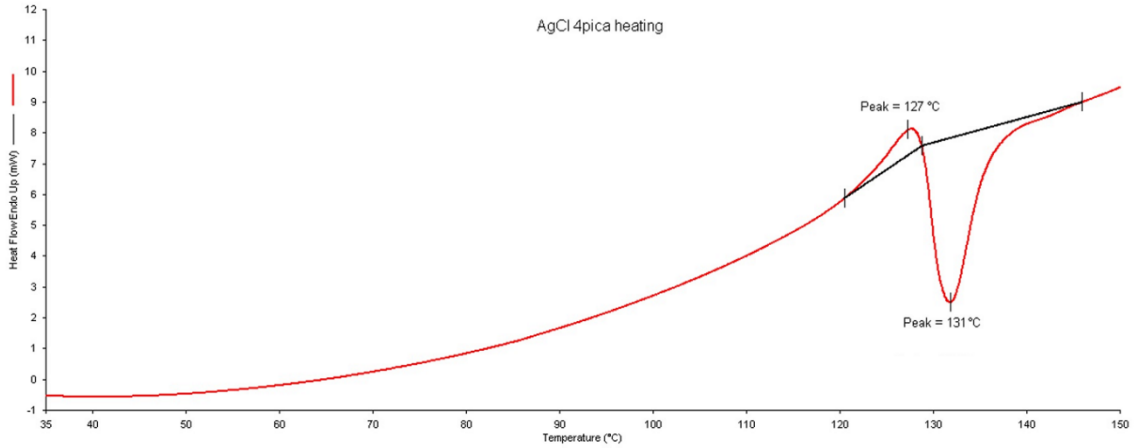

Fig. S29 DSC analysis of $[(AgCl)(4\text{-pica})]_n$. The endothermic peak at 127°C is followed by an exothermic peak at 131°C. Additional studies are required to fully characterize the system.

Solid state absorption and emission spectroscopy

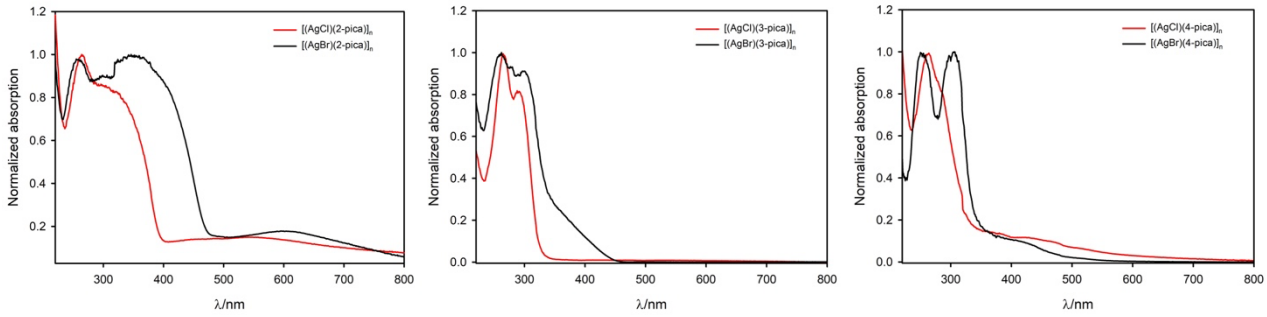

Fig. S30 Normalized absorption spectra of polymers $[(AgX)(2\text{-pica})]_n$ (left), $[(AgX)(3\text{-pica})]_n$ (middle) and $[(AgX)(4\text{-pica})]_n$ (right), with X = Cl, Br (red and black lines respectively), as powder at room temperature. Low-energy absorption features may be due to traces of metallic silver.

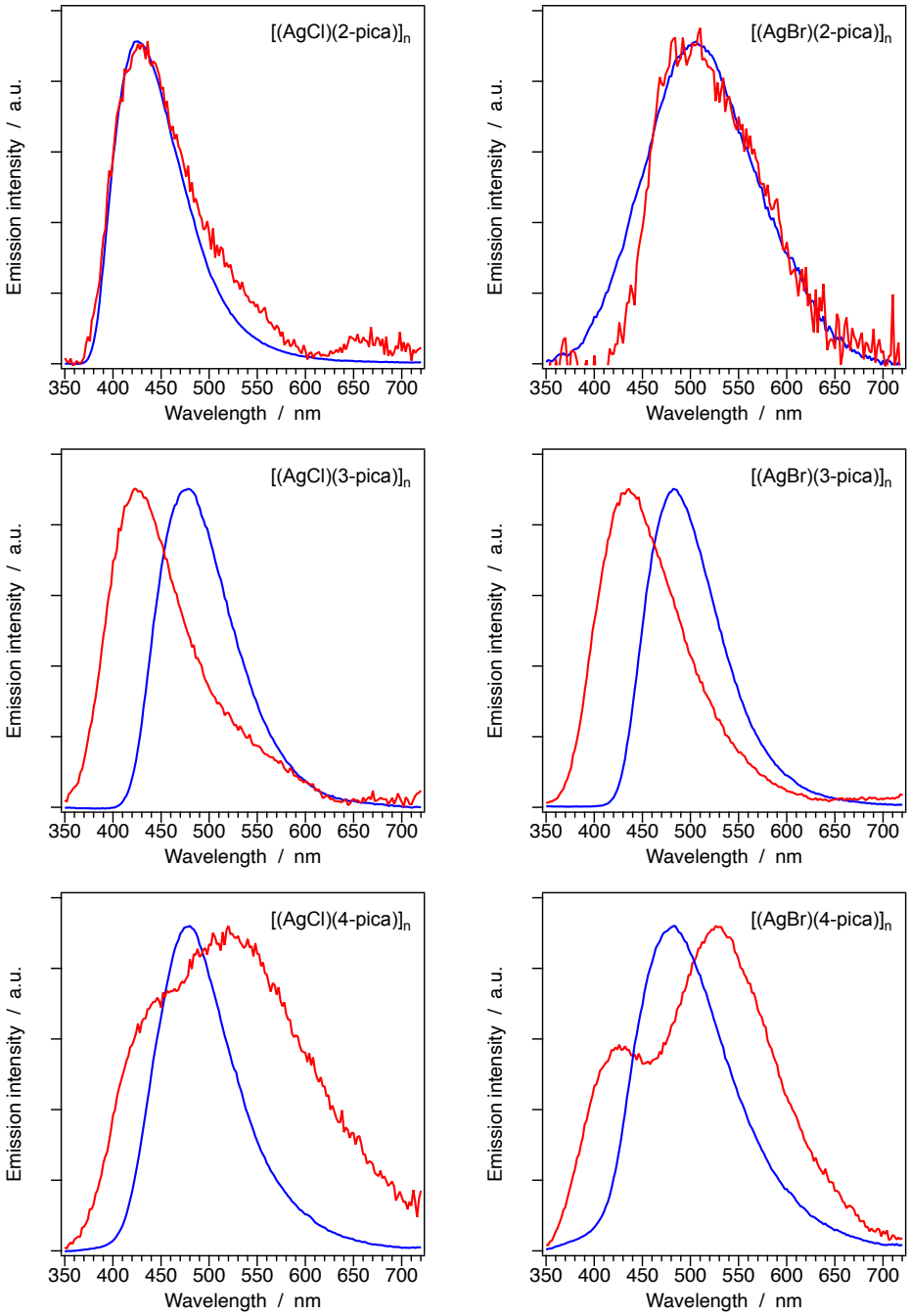

Fig. S31 Normalized emission spectra of all the investigated samples (as powder) recorded at 77 K (blue) and 298 K (red).

1 C. Zuffa, C. Cappuccino, M. Marchini, L. Contini, F. Farinella and L. Maini, *Faraday Discuss.*, 2023, **241**, 448–465.

2 I. Martina, R. Wiesinger and M. Schreiner, *e-Preservation Sci.*, 2012, **9**, 1–8.

3 M. Assis, F. C. Groppo Filho, D. S. Pimentel, T. Robeldo, A. F. Gouveia, T. F. D. Castro, H. C. S. Fukushima, C. C. de Foggi, J. P. C. da Costa, R. C. Borra, J. Andrés and E. Longo, *ChemistrySelect*, 2020, **5**, 4655–4673.